Accepted Manuscript

Unraveling Tensegrity Tessellations for Metamaterials with Tunable Stiffness and Bandgaps

Ke Liu, Tomás Zegard, Phanisri P. Pratapa, Glaucio H. Paulino

PII: S0022-5096(19)30043-2
DOI: https://doi.org/10.1016/j.jmps.2019.05.006
Reference: MPS 3623

To appear in: *Journal of the Mechanics and Physics of Solids*

Received date: 14 January 2019
Revised date: 11 May 2019
Accepted date: 12 May 2019

Please cite this article as: Ke Liu, Tomás Zegard, Phanisri P. Pratapa, Glaucio H. Paulino, Unraveling Tensegrity Tessellations for Metamaterials with Tunable Stiffness and Bandgaps, *Journal of the Mechanics and Physics of Solids* (2019), doi: https://doi.org/10.1016/j.jmps.2019.05.006

Unraveling Tensegrity Tessellations for Metamaterials with Tunable Stiffness and Bandgaps

Ke Liu[a], Tomás Zegard[b], Phanisri P. Pratapa[c], Glaucio H. Paulino[d,*]

[a]*Department of Mechanical and Civil Engineering, California Institute of Technology, Pasadena, CA 91125, United States*
[b]*Department of Structural & Geotechnical Engineering, Pontificia Universidad Católica de Chile, Chile*
[c]*Department of Civil Engineering, Indian Institute of Technology Madras, India*
[d]*School of Civil and Environmental Engineering, Georgia Institute of Technology, Atlanta, GA 30332, United States*

Abstract

Tensegrity structures resemble biological tissues: a structural system that holds an internal balance of prestress. Owing to the presence of prestress, biological tissues can dramatically change their properties, making tensegrity a promising platform for tunable and functional metamaterials. However, tensegrity metamaterials require harmony between form and force in an infinitely–periodic scale, which makes the design of such systems challenging. In order to explore the full potential of tensegrity metamaterials, a systematic design approach is required. In this work, we propose an automated design framework that provides access to unlimited tensegrity metamaterial designs. The framework generates tensegrity metamaterials by tessellating blocks with designated geometries that are aware of the system periodicity. We show that tensegrity metamaterials offer tunable effective elastic moduli, Poisson's ratio, and phononic bandgaps by properly changing their prestress levels, which provide a new dimension of programmability beyond geometry.

Keywords: tensegrity lattice, metamaterial, Class-1 tensegrity, tunable material properties, programmable materials

*Corresponding author
Email addresses: liuke@caltech.edu (Ke Liu), tzl@ing.puc.cl (Tomás Zegard), ppratapa@iitm.ac.in (Phanisri P. Pratapa), paulino@gatech.edu (Glaucio H. Paulino)

1 . Introduction

Biological tissues (such as muscles) are capable of actively changing their material properties [1, 2, 3]. Through the contraction of myofibrils, muscle cells generate prestress that lead to tunable stiffness and shape. This mechanism offers a route to create smart tunable materials. Tensegrity structural systems are known to mechanically resemble biological tissues [4, 5, 6], which have been shown to produce large changes in stiffness and shape [7]. Therefore, to a certain extent, we expect that if a material is composed of tensegrity micro-structures, then it can reproduce (or mimic) the behavior of biological tissues.

Tensegrities are structural systems with a continuous network of tensile members (i.e. cables), and disjointed compressive members (i.e. struts), whose integrity is maintained by self-balanced prestress in the cables and struts [8, 9, 10, 11, 12]. In engineering, a more general classification of tensegrity is proposed by Skelton & de Oliveira [10] where a Class-n tensegrity structure has at most n struts connected at each node. Under this expanded concept, the sculptures by Kenneth Snelson [13] belong to the Class-1 category. Engineering applications of tensegrities include deployable [14, 15, 7], actively tunable [16, 17, 18], and lightweight structures [19]. These advantages, if successfully transferred to the micro-scale, could lead to metamaterials with unprecedented mechanical properties and functionalities [9].

A straightforward way to make a metamaterial based on a tensegrity micro-structure is to tessellate a tensegrity unit cell in space to create a bulk assemblage (i.e. the metamaterial). Metamaterials based on lattice micro-structures have been used to create super lightweight materials. The mechanical properties and density of the metamaterials, as well as a wide range of other properties (e.g., acoustic, thermal, and biological properties), can be altered by adjusting the cellular architecture. This micro-lattice approach has led to lightweight materials that exhibit strength–stiffness ratios previously unachievable at low densities [20, 21, 22, 23].

Recently, a few pieces of pioneering work have shown that tensegrity metamaterials exhibit some unusual properties [24, 25, 26, 27, 28, 29, 30, 31]. Fraternali *et al.* [24] study solitary waves in a one-dimensional tensegrity chain composed of three-strut tensegrity prisms, indicating that such system might be used for impact mitigation. This one-dimensional system exhibits tunable frequency bandgaps when alternating tensegrity prisms with different height and stiffness are used [25]. Rimoli & Pal [26] investigate the mechanical properties of a tensegrity metamaterial design based on truncated octahedron elementary cells. They also observe that cable prestrains can sig-

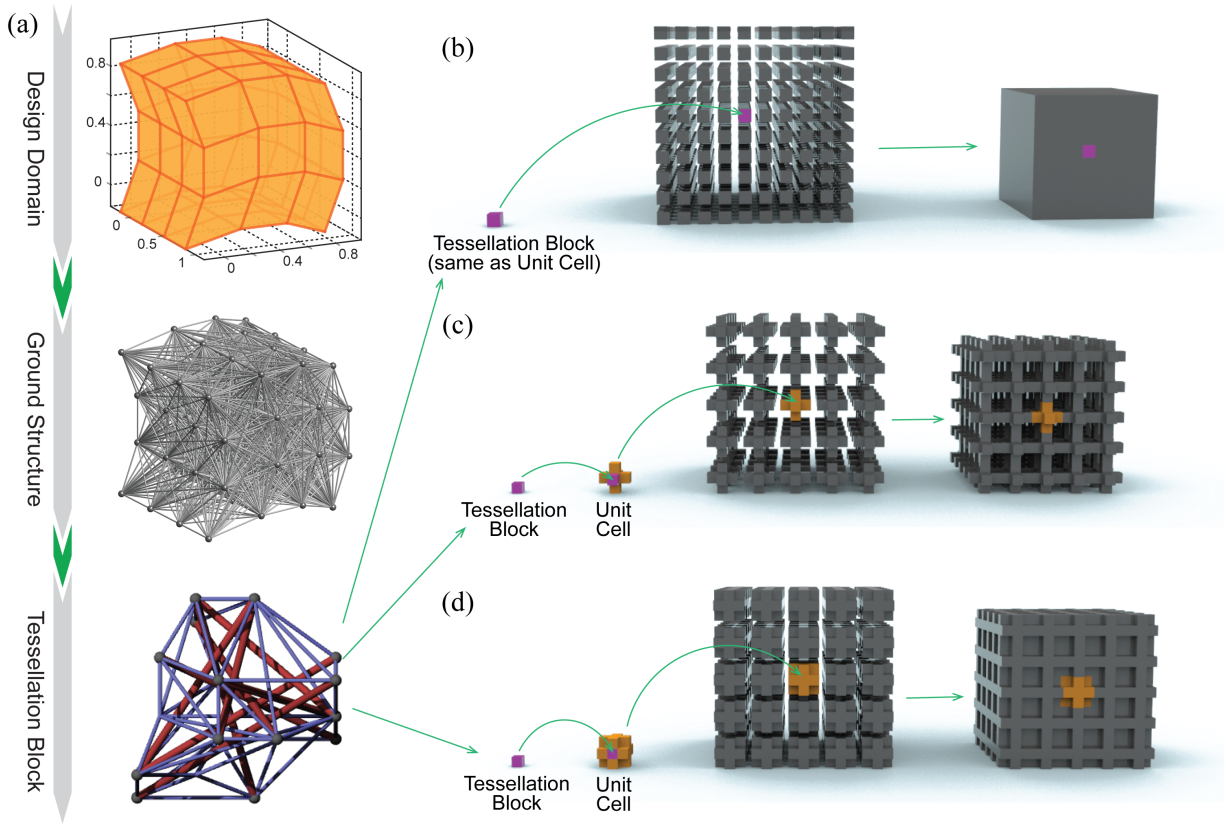

Figure 1: Schematic of the design framework to create tensegrity metamaterials. (**a**) From a (periodic) geometric design to a tensegrity tessellation block. (**b**)-(**d**) From tessellation block to tensegrity metamaterials. **(b)** The tessellation block is directly the unit cell for the bulk assembly, which is named as *dense tessellation*. **(c)** The tessellation block is first used to sub-assemble a porous unit cell which is re-tessellated into a bulk assembly, called the *porous tessellation*. This particular sub-assembled unit cell leads to truss-like assemblies. **(d)** The same tessellation block can be sub-assembled into different unit cells, leading to various *porous tessellations*. This particular *porous tessellation* is a honeycomb-like assembly.

nificantly affect the wave speeds in this tensegrity metamaterial [30]. However, these proposals of tensegrity metamaterials employ *ad hoc* designs; i.e. they are based on known stand-alone tensegrity designs that are not fully aware of the system periodicity once tessellated to become a metamaterial. This type of approach results in tensegrities of Class-2 or higher after the periodic tessellation. This limits control on the topological features of the tensegrity metamaterial, specifically its Class. Thus, the full potential of tensegrity metamaterials cannot be achieved. Moreover, the previously proposed approaches cannot lead to a Class-1 tensegrity tessellation. In practice, we are particularly interested at Class-1 tensegrity tessellations: they are easier to manufacture since they are composed of straight "struts" and "cables"; no special hinge is necessary since two struts never intersect; the structure is less likely to develop undesirable bending forces in the struts; large deformations in the system (shortening of the struts) due to prestress or service loads are

easier to account for; etc. Thus, there is a need for a systematic approach to design tensegrity metamaterials with a desired unit cell geometry and Class category – this is our focus.

Multiple approaches exist for the design of stand-alone tensegrities [32, 33, 34, 35, 36, 37, 38, 39, 40, 41, 42, 43]. However, it is challenging to incorporate periodicity in these approaches, especially concerning the topology of the design. To overcome these challenges, we propose a design framework that can automatically create tensegrity-based metamaterials with periodic unit cells, as illustrated by Fig. 1. The framework utilizes topology optimization to find tensegrity tessellation blocks with prescribed tiling geometries (periodicity). The resulting units can be tessellated, either densely or porously, to create metamaterials. Using this automated process, we can create a library of tensegrity metamaterial designs (see Table A.1). The following key terms are used in this manuscript: *tessellation block*, the building block of a tessellation unit cell; *design domain*, the geometric space within which the tensegrity (tessellation block) is designed; *unit cell*, the periodic micro-structure of the tensegrity metamaterial. To demonstrate the applications of the proposed approach, we use one example from the obtained tensegrity tessellation blocks to create both, densely and porously tessellated Class-1 tensegrity metamaterials. We investigate their static properties through homogenization, and dynamic properties through Bloch wave analyses. We show that the effective elastic moduli, Poisson's ratio, and phononic bandgaps of the tensegrity metamaterials can be effectively tuned by changing prestress level, our design parameter of interest.

2 . Topology design formulation

Let us start with the design of stand-alone tensegrity structures, which will form the basis to the design of metamaterials. The conceptual design of a tensegrity consists of three essential components: topology (i.e. connectivity), geometry (i.e. configuration), and self-balanced prestress state. Most numerical design methods start with a given topology for the tensegrity and evolve its geometry to achieve a self-balanced prestress state [44, 35, 33]. More recently, design approaches which manipulate the topology have been explored [37, 38, 39, 40, 41, 42, 43]. These instead, seek the proper topology that allows for a self-balanced prestress state within a given geometry. From a designer's point of view, the geometry of a structure is typically given or constrained, and thus the topology design approach is more intuitive. In addition, for complex designs, it is difficult to define the initial (fixed) topology for the geometry-based approaches.

In the present work, we propose an optimization formulation for topology design of tensegrity

structures based on the ground structure method and force maximization with arbitrary geometries [43]. The ground structure method has been extensively used in the field of (structural) topology optimization [45, 46, 47, 48]. It provides a very dense (and redundant) set of potential candidate members and joints, from where the final structure can be extracted through an optimization process. In the topology optimization of tensegrities, this process involves finding the associated self-balanced prestress forces as well. The joint coordinates are fixed during the optimization, thus preserving the prescribed geometry of the tensegrity.

Let us denote $\mathbf{t}$ as the tension forces in all candidate members, and $\mathbf{c}$ the compression forces. The real force in a member is therefore $(\mathbf{t}-\mathbf{c})$. By decoupling tension and compression, we obtain two vectors of non-negative design variables, each of size $N_{E_g} \times 1$, where N_{E_g} is the number of candidate members provided by the ground structure. The binary design variables $\mathbf{s}$ indicate the presence of struts: $s_k = 1$ indicated that the k-th candidate member is a strut (as opposed to a cable). Eventually, the optimization formulation is written as a mixed integer linear programming (MILP) problem:

$$\max_{\mathbf{t},\mathbf{c},\mathbf{s}} \quad \mathbf{1}^{\mathbf{T}}(\mathbf{t}-\mathbf{c}) \tag{1a}$$

$$\text{s.t.} \quad \mathbf{B}(\mathbf{t}-\mathbf{c}) = \mathbf{0} \tag{1b}$$

$$\mathbf{G}\mathbf{s} \leqslant n\mathbf{1} \tag{1c}$$

$$\mathbf{G}_p\mathbf{s} \leqslant \mathbf{1} \tag{1d}$$

$$\mathbf{1}^T\mathbf{s} \leqslant N_{S,max} \tag{1e}$$

$$\mathbf{0} \leqslant \mathbf{t} \tag{1f}$$

$$\mathbf{0} \leqslant \mathbf{c} \leqslant \mathbf{s} \leqslant \mathbf{1} \tag{1g}$$

$$\mathbf{s} \in \mathbb{Z}^{N_{E_g}} \tag{1h}$$

The constraints restrict the solution space to feasible tensegrity designs. Eq. (1b) requires self-balance of prestress forces, where $\mathbf{B}$ is the equilibrium matrix [11]. Eq. (1c) imposes discontinuity of struts. The incidence matrix $\mathbf{G}$ is defined as:

$$G_{ij} = \begin{cases} 1, & \text{if member } j \text{ is connected to node } i \\ 0, & \text{otherwise} \end{cases} \tag{2}$$

Thus $\mathbf{G}$ is a $N_{V_g} \times N_{E_g}$ binary matrix which contains the connectivity information, i.e., the topology, of a ground structure, where N_{V_g} refers to the number of nodes in the ground structure. Each column of $\mathbf{G}$ contains exactly two entries of value 1, with the row indices indicating the start/end nodes of a member. The product $\mathbf{Gs}$ results in an $N_{V_g} \times 1$ vector whose entries indicate the numbers of struts connected to each node, which need to be smaller than the Class number n. Eq. (1d) prevents collisions between struts to improve manufacturability of the design, which is defined as:

$$G_{p,ij} = G_{p,ik} = \begin{cases} 1, & \text{if members } j \text{ and } k \text{ collide with each other at incidence } i, \\ 0, & \text{otherwise.} \end{cases} \tag{3}$$

The $\mathbf{G}_p$ matrix is defined such that, if the product $\mathbf{G}_p\mathbf{s}$ leads to any entry greater than 1, then there are two struts colliding with each other in space. In this work, each row of $\mathbf{G}_p$ corresponds to a fictitious point reporting an intersection of the centerlines of two members. For more details on the definition of the matrix $\mathbf{G}_p$, the reader is referred to reference [43], which includes an example in Appendix 2. Eq. (1e) limits the number of struts (denoted as N_S) in a tensegrity design by $N_{S,max}$. Eqs. (1f) to (1h) define bounds for the design variables, among which Eq. (1g) also ensures that the strut indicator is 1 when an element takes the form of a strut.

This formulation is able to effectively reproduce many of the renowned tensegrities, and create new stable tensegrities [43]. However, directly applying Formulation (1) for designing tessellation blocks for tensegrity metamaterials will not produce desired results. The reason being that tensegrity metamaterials are periodic tessellations of the unit cells: the periodicity of tessellation block must be considered in the formulation. The periodicity leads to shared nodes on the common boundaries of each tessellation block, which makes our strut discontinuity constraint defined in Eq. (1c) ineffective, as sketched in Fig. 2(a). Therefore, the periodic boundary conditions (PBCs) must be included in the strut discontinuity constraint (1c), as shown in Fig. 2(b). For the self-balance constraint in Eq. (1b) the PBCs are not enforced: a self-balanced tessellation block (naturally) results in a self-balanced periodic assembly. Hence, there is no force flowing between adjacent tessellation block in a tensegrity for metamaterial design. This leads to an unintended advantageous property: a finite assembly of tessellation blocks does not require additional support over its boundary to maintain the equilibrium of the (metamaterial) system.

To incorporate the PBCs, we need to identify the common nodes on the tessellation block's

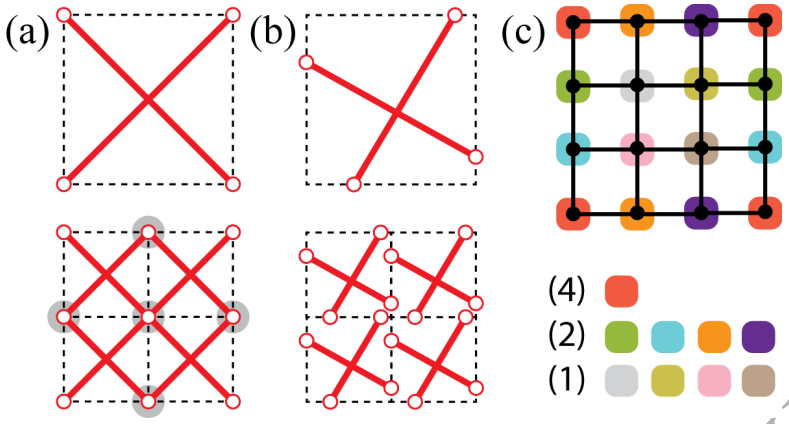

Figure 2: Effect of periodic boundary condition on the topology of struts. **(a)** Tessellating Class-1 tessellation block creates nodes connecting multiple struts, which is not desired. The red bars indicate struts. If the struts are placed as shown in **(b)**, the tessellation preserves the tessellation block's Class category – there is no pair of struts connected at one node. (Note: intersections within the length of struts is ignored in this demonstration) **(c)** Identification of independent groups of nodes for a 4×4 ground structure. Different groups are identified by different colours. The numbers in parenthesis provide the numbers of nodes in different groups. The 4 corner nodes belong to the same group.

boundaries. There are several independent groups of nodes: each group contains the indices of nodes that are images of each other under translational symmetry (i.e. periodicity). For example, two nodes belong to the same group if their coordinates satisfy:

$$\mathbf{x}_j = \mathbf{x}_i + (n_1\boldsymbol{a}_1 + n_2\boldsymbol{a}_2 + n_3\boldsymbol{a}_3), \quad n_1, n_2, n_3 \in \{-1, 0, 1\}. \tag{4}$$

where $\mathbf{x}_i$ and $\mathbf{x}_j$ denote the coordinates of nodes i and j, respectively; while $\boldsymbol{a}_1$, $\boldsymbol{a}_2$, and $\boldsymbol{a}_3$ are the three primitive vectors of the tessellation. Node groups may be of different size under translational symmetry – we refer to Fig. 2(c) for a 2D example. As an example, in a cubic design domain, the 8 corner nodes belong to the same group. It should be noted that an internal node belongs to an independent group by itself. Nodes can be classified into independent groups algorithmically, which is elaborated in Appendix B. After generating the node groups, an identification matrix $\mathbf{Q}$ can be constructed as:

$$Q_{ij} = \begin{cases} 0, & \text{if node } j \text{ does not belong to group } i \\ 1, & \text{if node } j \text{ belongs to group } i. \end{cases} \tag{5}$$

The number of rows of $\mathbf{Q}$ equals to the number of independent groups, and the number of columns equals to the total number of nodes in the ground structure. For tensegrity metamaterial designs,

the strut discontinuity of a tessellation block (tensegrity Class) is counted for each independent group, as opposed to individual nodes. Using the identification matrix $\mathbf{Q}$, we can rewrite Eq. (1c) for tensegrity metamaterial design as:

$$\mathbf{QGs} \leqslant n\mathbf{1}. \tag{6}$$

which is an elegant constraint to achieve the intended metamaterial design. We note that, in general, the obtained tensegrity tessellation block designs do not display any apparent symmetry. In particular, reflection symmetry is not allowed if the design needs to be globally Class-1, as implied by the schematics in Fig. 2.

3 . Geometry of design domain

To perform the topology optimization, we need to build a ground structure, which is generated by a set of nodes that conforms to prescribed geometries. Our experience shows that *balloon-like* domains are likely to result in better tensegrity designs. In that regard, we develop a set of algorithms and tools with the purpose of making the design domains simple to define and manipulate (i.e. the nodes of the ground structure). The goal of these algorithms is not to span the infinitely rich space of potential tessellation block geometries; but provide enough design freedom and easy-usage to allow for a large variety of designs to be conceived. The described algorithm for generating the unit geometry is summarized by the simplified flowchart in Fig. 3(a).

After a unit geometry is defined, a second set of transformations and variations can be applied. These transformations and variations are based on: (a) inner holes, and (b) morphing of the geometry. These are also parametrized, and thus the space of design domains for tensegrities (while not infinite) is reasonably large.

The simplest manner to define a polyhedron is by using only the vertices and making the polyhedron the convex hull of these [49, 50]. If the polyhedron is tessellated, a set of primitive vectors that replicate the unit and span the entire space must also be defined. Thus, the required user input to define a design domain consists of two pieces of information: (a) spatial nodes (vertices) defining the boundary of the design domain; (b) a set of primitive vectors which span the three-dimensional space.

As demonstrated in Fig. 2, extra nodes within the connecting facets are also needed in addition to the basic (convex hull) vertices. This is necessary to allow freedom of the strut layout. These

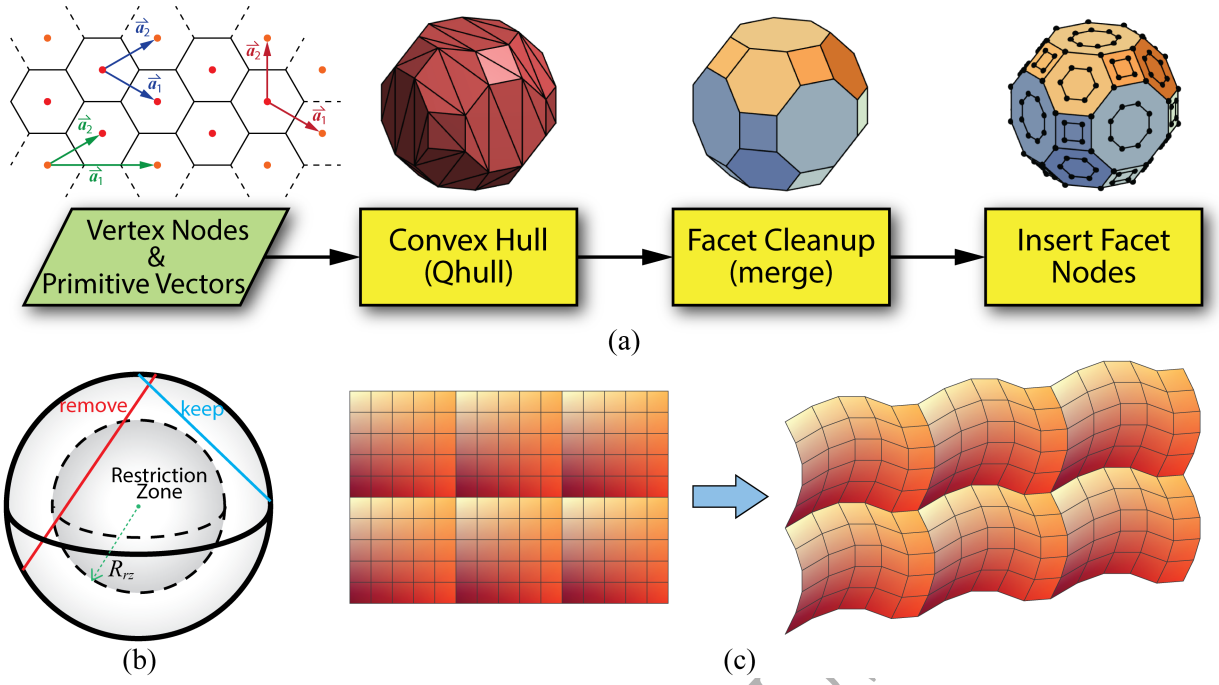

Figure 3: Creation of the design domain (i.e. geometry of the tessellation block). **(a)** Domain unit-cell generation based on convex hulls. The black dots are the nodes used to generate the ground structure for topology optimization. **(b)** Restriction zone creates holes in the design domain (i.e. the ground structure) by removing all members across the prescribed zone(s). **(c)** Morphing example: original (un-morphed) tessellation block and morphed tessellation block (in 2×3 assemblies).

additional facet nodes can be added in a parametric manner, for instance, by shrinking the facet boundary and including these (shrunk) vertices in the domain. However, it should be noted that other options are available and can be easily implemented.

The tensegrity topology optimization formulation can handle concavities and even holes (or voids) in the domain. While the nature of the convex-hull approach does not result in tessellation blocks with concavities, the addition of inner holes (or concavities) as a subsequent step is possible (optional), and is fully compatible with the topology optimization formulation. This feature leads to a better tuning of the resulting micro geometry of the tessellated metamaterial. The inner hole and concavities use the concept of *restriction zones* [47, 48], as illustrated in Fig. 3(b). Typically, a spherical restriction zone with radius R_{rz} centered at the centroid of the unit geometry is used.

Additional variations for a given unit geometry and primitive vectors can be achieved by morphing: the geometry of a tessellation block (and its primitive vectors) can be "deformed" (in a virtual sense) while keeping their space-spanning property. Fig. 3(c) illustrates a two-dimensional example of a square design domain being morphed into a new design domain, while keeping its space-spanning property.

4 . Variations of tessellation strategy

We explore different strategies to tessellate the obtained tessellation blocks. The tensegrity tessellation block obtained by topology optimization (see Section 2) from the unit geometry (as defined in Section 3) can be directly tessellated in space in accordance to the primitive vectors to make the metamaterial bulk assembly, as illustrated in Fig. 1(b). Moreover, it should be noted that these primitive vectors are often not unique: any set of vectors that span the entire space and correctly tessellate the tessellation block (no overlaps) are valid, as long as the nodes in some of the facets are common among neighboring units. We also note that it is not required for the tessellation to be *space filling*, i.e. to completely fill the three-dimensional space: voids may be left in the tessellation. Therefore, we can explore porous strategies to tile the tessellation block in order to achieve different bulk assemblies. Furthermore, owing to the self equilibrium of the tessellation block (refer to Section 2), units can be removed from the bulk assembly without compromising the stability of the system: i.e. holes can be intentionally left in the tessellation.

A porous tessellation can be constructed as follows: the tessellation block is tessellated a few times in a porous manner (i.e. leaving certain positions empty); this porous unit cell is then re-tessellated to make metamaterial bulk assemblies, as demonstrated in Figs. 1(c) and (d). The porous unit cell is encoded by a three-dimensional array $\mathbf{N}_s$ of size $N_{s1} \times N_{s2} \times N_{s3}$ with `true`/`false` values. The tessellation block is then tessellated along each of the 3 primitive vectors, but a structure is only created/appended to the unit cell when a `true` is found. This is repeated for all three primitive vectors (all three dimensions of $\mathbf{N}_s$). Thus, the same tensegrity tessellation block can result in various metamaterials; either by itself or in a sub-assembled unit cell. The sub-assembly approach is general: a single `true` value in $\mathbf{N}_s$ (matrix of size $1 \times 1 \times 1$) refers to the original case when no porous unit cell is used to create a densely tessellated metamaterial.

4 .1. Stiffness matrix of tensegrity

By definition, tensegrity structures have a self-balanced prestress: the initial undeformed configuration of a tensegrity structure is in reality a deformed state of its base materials. Thus, based on this line of reasoning, we establish the stiffness matrix of a tensegrity structure following an Updated Lagrangian formulation. In this sense, the deformation of a tensegrity structure refers to the prestressed configuration, which is obtained from topology optimization in the present framework. We briefly go through the derivation of the (tangent) stiffness matrix of a tensegrity in this

section. As a matter of notation, we use left-subscript to label the reference configuration of a quantity, and left-superscript to label the configuration when the quantity is evaluated (or occur).

By means of the principle of virtual work, the linearized equilibrium of a deformed one-dimensional elastic rectilinear element is given by [51]:

$$\int_{_1V}({}_1E)({}_1e_{11})\delta({}_1e_{11})d^1V+\int_{_1V}({}^1\sigma_{11})\delta({}_1\eta_{11})d^1V=\int_{_1S}{}^2_1t\delta ud^1S-\int_{_1V}({}^1\sigma_{11})\delta({}_1e_{11})d^1V \tag{7}$$

where, ${}^1V$ denotes the prestressed configuration, ${}_1E$ is the tangent elastic modulus, ${}_1e_{ij}$ and ${}_1\eta_{ij}$ are the linear and nonlinear components of the incremental Green-Lagrange strain (denoted as ${}_1\varepsilon_{11}$) defined on the prestressed configuration, and ${}^1\sigma_{11}$ is the Cauchy stress which is also defined on the prestressed configuration (Fig. 4(a)). The unknown displacement variation is denoted as δu, and ${}^2_1t$ is the deformation independent boundary traction vector (measured per unit boundary area at the prestressed state). Considering uniform strain and stress within an element, the incremental Green-Lagrange strain can be expressed as a function of nodal displacements of member r (denoted as $\mathbf{u}_r$) upon the prestressed configuration. The linear (${}_1e_{ij}$) and nonlinear (${}_1\eta_{ij}$) components of ${}_1\varepsilon_{11}$ are given by:

$${}_1e_{11}=\frac{1}{{}^1L_r}\mathbf{B}_L^T\mathbf{u}_r,\qquad {}_1\eta_{11}=\frac{1}{2({}^1L_r^2)}\mathbf{u}_r^T\mathbf{B}_{NL}\mathbf{u}_r, \tag{8}$$

where,

$$\mathbf{u}_r=[\ \mathbf{u}_a^T,\ \mathbf{u}_b^T]^T,\quad \mathbf{u}_i={}^2\mathbf{x}_i-{}^1\mathbf{x}_i\ \ (i=a,\ b),\quad L_r=\|{}^1\mathbf{x}_b-{}^1\mathbf{x}_a\|, \tag{9}$$

$$\mathbf{B}_L=\frac{1}{L_r}\Big[{}^1\mathbf{x}_a^T-{}^1\mathbf{x}_b^T,\ \ {}^1\mathbf{x}_b^T-{}^1\mathbf{x}_a^T\Big]^T,\quad \mathbf{B}_{NL}=\begin{bmatrix}+\mathbf{I}_3 & -\mathbf{I}_3\\ -\mathbf{I}_3 & +\mathbf{I}_3\end{bmatrix}. \tag{10}$$

We remark that $\mathbf{u}_r$ is measured taking reference to the prestressed configuration. Substituting Eq. (8) into Eq. (7), the equilibrium of the system can be discretized and rewritten in matrix form as:

$$\delta\mathbf{u}_r^T\mathbf{K}_{re}\mathbf{u}_r+\delta\mathbf{u}_r^T\mathbf{K}_{rg}\mathbf{u}_r=\delta\mathbf{u}_r^T{}^2_1\mathbf{f}_r-\delta\mathbf{u}_r^T{}^1_1\mathbf{f}_r \tag{11}$$

where $\mathbf{K}_{re}$ is the elemental elastic stiffness matrix, and $\mathbf{K}_{rg}$ is the elemental geometric stiffness

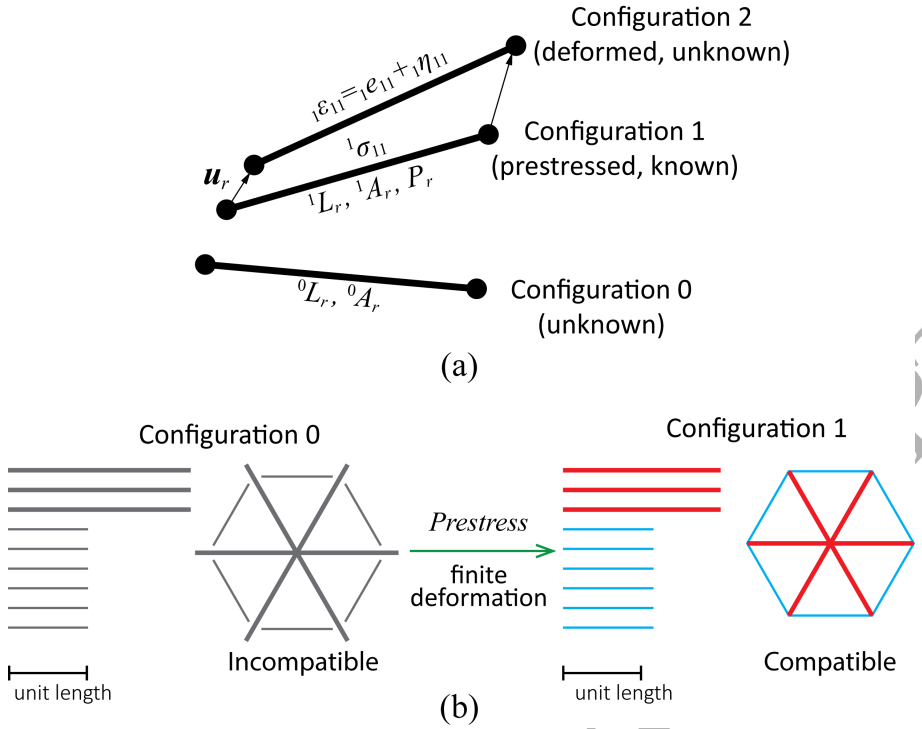

Figure 4: Illustration of the Updated Lagrangian formulation for the derivation of the stiffness matrix of a tensegrity. **(a)** Individual member configurations. Configuration 0 is the initial undeformed configuration; Configuration 1 is the prestressed configuration; and Configuration 2 is the deformed configuration upon the prestressed configuration. Only the prestressed state is known. **(b)** Configurations of members with respect to the tensegrity structure. The stiffness matrix is formulated upon Configuration 1. Large deformation of each individual member is allowed between Configuration 0 and Configuration 1. Notice that the members in Configuration 0 may not be compatible to allow structural integrity. An integral structure only appear in Configuration 1 when all members are properly prestressed.

matrix. They are derived as:

$$\mathbf{K}_{re} = \frac{({}_1E_r)({}^1A_r)}{{}^1L_r}\mathbf{B}_L\mathbf{B}_L^T, \tag{12}$$

$$\mathbf{K}_{rg} = \frac{({}^1\sigma_{11})({}^1A_r)}{{}^1L_r}\mathbf{B}_{NL}. \tag{13}$$

Because we adopt the Updated Lagrangian approach, the obtained elemental stiffness matrix reflects a tangent state of the prestressed member, and this approach does not require compatibility (structural integrity) of the structure from the initial rest configuration to the prestressed configuration (see Fig. 4(b)). The external applied forces ${}^2_1\mathbf{f}_r$ to the prestressed element comes from the first term of the right hand side of Eq. (7), which is usually directly applied to nodes, and thus there is no need to carry out the integration. The second term of the right hand side of Eq. (7)

provides the nodal forces due to the internal prestress, which are given by:

$$ {}^{1}_{1}\mathbf{f}_r = ({}^{1}\sigma_{11})({}^{1}A_r)\mathbf{B}_L. \tag{14} $$

According to the design obtained from our topology optimization formulation (see Section 2), we choose the values of $({}^{1}L_r)$ and $({}^{1}\sigma_{11})({}^{1}A_r)$, where the later term is the prestress force (i.e. $P_r = ({}^{1}\sigma_{11})({}^{1}A_r)$) of member r. Let's assume ${}^{1}E_r = E_r$. We can define ${}^{1}A_r$ to be proportional to P_r such that the magnitude of ${}^{1}\sigma_{11}$ is uniform for all members (i.e. fully stressed design). Now, assuming a constant Young's modulus such that ${}^{1}E_r = {}^{0}E_r = E_r$, the original cross sectional area of a member (before prestress is applied) can be determined by solving the following equation:

$$ {}^{1}A_r = \left(1 - \frac{\nu P_r}{{}^{0}A_r E_r}\right)^2 ({}^{0}A_r) \tag{15} $$

where ν is the Poisson's ratio of the base material (assumed constant). We remark that, in the Updated Lagrangian formulation, all the input parameters to the stiffness matrix are defined based on the prestressed configuration (i.e. Configuration 1). Because we perform elastic analysis, these quantities do not have any history dependence on the initial configuration (i.e. Configuration 0). Therefore, large deformation is allowed between the initial configuration (rest lengths) and the prestressed configuration (current lengths). According to this line of reasoning, even if we assume E_r as constant, the material does not behave like a conventional linear spring, which is due to the change of reference configuration during the deformation.

Assembling Eq. (11) over all elements in the structure and admitting the arbitrary nature of the virtual displacement ($\delta\mathbf{u}$), we obtain the incremental finite element equation of the entire structure:

$$ \mathbf{K}\mathbf{u} = (\mathbf{K}_e + \mathbf{K}_g)\mathbf{u} = {}^{2}_{1}\mathbf{f} - {}^{1}_{1}\mathbf{f}. \tag{16} $$

Notice that a self-equilibrating tensegrity structure requires that ${}^{1}_{1}\mathbf{f} = \mathbf{0}$. For linear elastic analysis, we assume that the cables do not slack.

5 . Tunable elastostatic properties

Assuming the unit cell dimension is sufficiently small compared to the macroscale dimension of the metamaterial, we can obtain the effective properties of the tensegrity metamaterial through

homogenization [52]. We use computational homogenization to obtain the effective properties of a tensegrity metamaterial based on the unit cell. Periodic boundary conditions (PBCs) are applied to a tensegrity unit cell [53], such that:

$$\mathbf{u}_m - \mathbf{u}_s = (\mathbf{F} - \mathbf{I})({}^1\mathbf{x}_m - {}^1\mathbf{x}_s), \qquad \mathbf{f}_m + \mathbf{f}_s = \mathbf{0}, \tag{17}$$

which represent periodic deformations and anti-periodic tractions on the boundaries of the unit cell. The subscripts m and s refer to master and slave nodes on opposite boundaries. The nodal displacements of a master-slave pair are $\mathbf{u}_m$ and $\mathbf{u}_s$. The nodal positions in the prestressed state are ${}^1\mathbf{x}_m$ and ${}^1\mathbf{x}_s$, which equals to the primitive vector of the lattice in the corresponding direction of the two nodes. The symbol $\mathbf{F}$ denotes the deformation gradient of the homogenized material. In linear analysis, these two boundary conditions can be directly condensed into the stiffness matrix and force vectors. Following the procedure proposed by Vigliotti & Pasini [53], we derive the full homogenized linear elasticity tensor $\mathbf{D}$ of the tensegrity metamaterial. We use the reduced format (Voigt notation) of the elasticity tensor, and thus, $\mathbf{D}$ is a 6×6 symmetric matrix. The computational implementation is elaborated upon in Appendix C.

To demonstrate how the elastic properties of a tensegrity metamaterial can be tuned, we refer to Table A.1 and select the tessellation block design based on the cuboctahedron geometry (composed with 13 struts and 96 cables) as an example. Analyzing the null space of the equilibrium matrix $\mathbf{B}$ in Eq. (1b), we find that there are 12 independent prestress states that can possibly exist given the layout of the tensegrity block. The current prestress state that we obtained from the topology optimization is a linear combination of the many independent states that maximizes the sum of forces within members. In addition, the cuboctahedron tessellation block possesses 17 independent internal mechanisms (i.e. degree of kinematic indeterminacy), which are stabilized by the current prestress assignment. To demonstrate the richness of our design space, the cuboctahedron tessellation block is used to create two Class-1 tensegrity metamaterial designs: one using a dense tessellation (see Fig. 5(a) and Supplementary Video S1); and a second one with a porous tessellation (Fig. 5(b)). According to Figs. 5(d) to (f), we can clear observe that no pair of struts are connected between tensegrity blocks. We denote the Young's modulus of strut material as E_S, and cable material as E_C. The areas of other struts and cables are determined proportionally based on the prestress forces. We find that all struts in the cuboctahedron tessellation block have the same prestress forces, while the cables are sized to ensure uniform magnitude of stress (${}^1\sigma_{11}$)

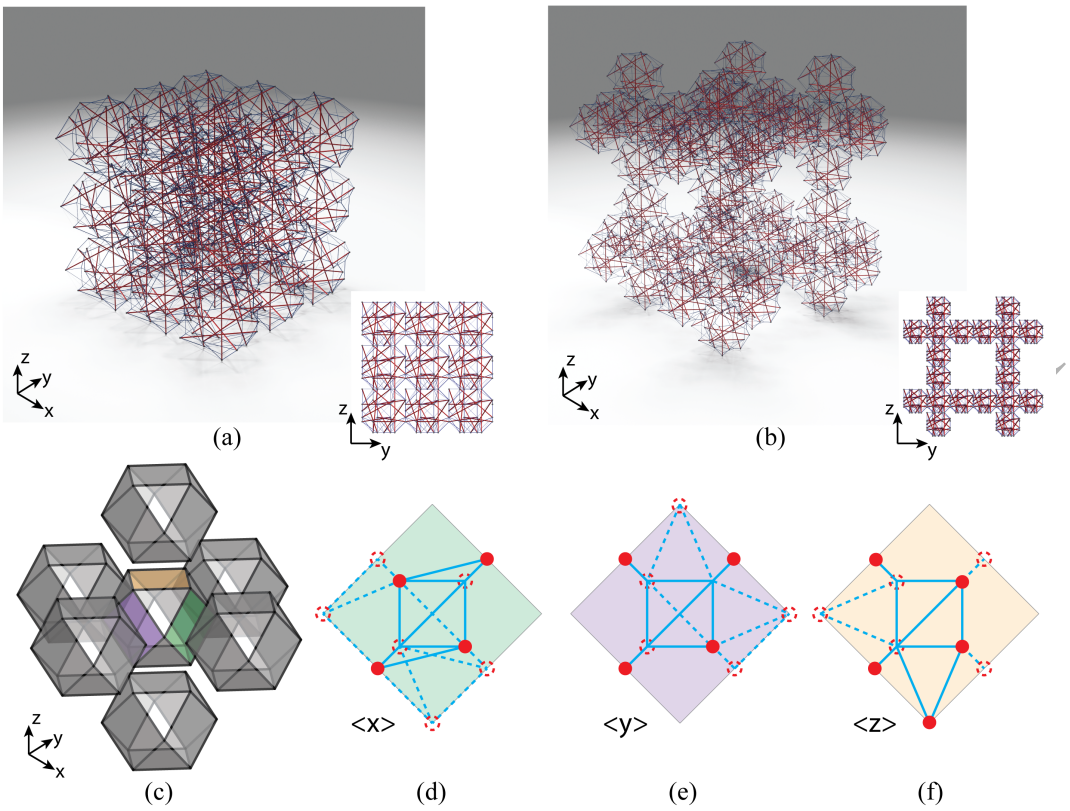

Figure 5: Tessellating tessellation block to obtain tensegrity metamaterials – see "Cuboctahedron" example of Table A.1. **(a)** Demonstration of the dense tessellation using the cuboctahedron tessellation block. **(b)** Demonstration of a porous tessellation based on the same tessellation block. **(c)** Illustration of the shared interfaces between adjacent blocks in three primitive directions. The green, purple, and gold faces refer to the interfaces in the x, y, and z directions, respectively. **(d)-(f)** Detailed layout of the interfaces. Background colors are in correspondence with face colors in (c). The filled red dot and dashed red circles indicate nodes connected with struts, and the continuous and dashed blue lines indicate cables within the boundary layer. We use filled (continuous) and dashed objects to distinguish their belongings to the two adjacent tessellation blocks.

in all of them (fully stressed design).

In all simulations, we have used a linear elastic model with material parameters: Young's moduli of struts $E_S = 2600$MPa, Young's moduli of cables $E_C = 12$MPa, and mass density for both $\rho = 1.18 \times 10^{-3}$g/mm^3, which are the typical properties of polymers used in 3D printing. We consider a cuboctahedron unit cell bounded in a 10mm$\times$10mm$\times$10mm box. We assume that all members have a circular cross-section, and the maximum radius of struts is $r = 0.5$mm in the prestressed state, and hence ${}^1A_S = 0.25\pi$mm^2. This work does not consider geometric changes of the tensegrity metamaterials due to varying external stimuli, i.e. we assume that the prestressed configurations of the tensegrity metamaterial under different prestress level are within infinitesimal (linear) deformations, and thus can be ignored.

If we assume that the prestress in the metamaterial is ${}^1\sigma_{11} = (0.05E_C) = 0.60$MPa, we can

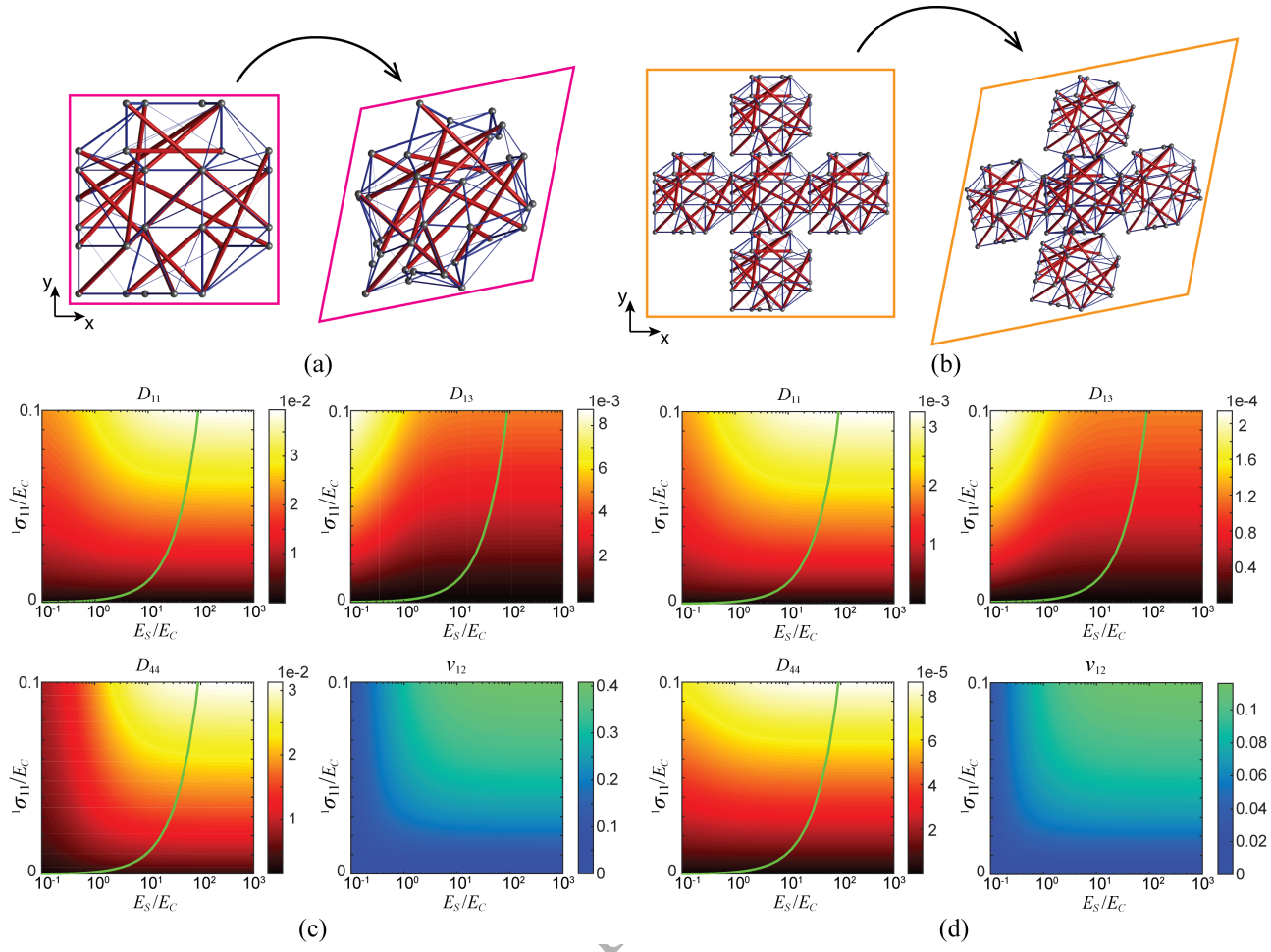

Figure 6: Tensegrity metamaterial with tunable elastic properties. **(a)-(b)** Undeformed and simply sheared modes of the two metamaterials unit cells: **(a)** Densely tessellated metamaterial, **(b)** Porously tessellated metamaterial. **(c)-(d)** Tunable elastic properties (including elastic modulus D_{11}, D_{13}, D_{44}; and Poisson's ratio ν_{12}): **(c)** Densely tessellated metamaterial, **(d)** Porously tessellated metamaterial. The green lines indicate the limit of prestress that may cause buckling of struts. To the right of the green line, buckling is unlikely to happen.

obtain the homogenized elasticity tensor of the *densely tessellated metamaterial* (see Fig. 5(a)) as:

$$\mathbf{D}_{dense} = \begin{bmatrix} 23.76 & 4.90 & 2.69 & 0.10 & 1.06 & -1.79 \\ & 17.03 & 2.65 & 2.07 & -0.60 & 1.71 \\ & & 23.48 & 1.41 & -3.26 & -2.95 \\ & & & 20.48 & 1.07 & 2.64 \\ & \textit{symm.} & & & 13.93 & 4.82 \\ & & & & & 14.38 \end{bmatrix} \times 10^{-3}\ \text{MPa}. \tag{18}$$

Moreover, the homogenized elasticity tensor of the *porously tessellated metamaterial* (see Fig. 5(b))

is given by:

$$\mathbf{D}_{porous} = \begin{bmatrix} 20.73 & 1.38 & 0.76 & -0.07 & -0.05 & -0.06 \\ & 15.68 & 0.69 & 0.10 & -0.01 & -0.08 \\ & & 22.33 & -0.05 & 0.02 & -0.03 \\ & & & 0.48 & 0.04 & 0.01 \\ & symm. & & & 0.46 & 0.03 \\ & & & & & 0.45 \end{bmatrix} \times 10^{-4} \text{ MPa}. \tag{19}$$

We observe that both metamaterials exhibit anisotropy. The porously tessellated tensegrity metamaterial is much softer than the densely tessellated metamaterial, especially in shear. The unit cell deformations under a simple shear of the two metamaterials are illustrated in Figs. 6(a) and (b).

Figs. 6(c) and (d) show how some of the elastic moduli change in response to various material properties and prestress level (normalized by E_C). The densely tessellated metamaterial has a much larger Poisson's ratio (in the xy-plane) than the porously tessellated one, when the prestress level is high. The tunability due to variations in the prestress is more effective when compression members are much stiffer than tension members: changes of diagonal moduli of the elasticity tensor are more sensitive to changes in the prestress level when $E_S/E_C > 10^2$. In addition, when $E_S/E_C > 10^2$, buckling of compression members (i.e. struts) is unlikely to happen. Considering Euler buckling [54], the stress of the longest compression member (with circular cross section) should satisfy:

$$^1\sigma_{11} \leq \frac{\pi E_S (^0A_{Smin})}{4\,^0L_{Smax}^2} \leq \frac{\pi E_S (^1A_{Smin})}{4\,^1L_{Smax}^2}, \tag{20}$$

where $^0A_{Smin}$ (and $^1A_{Smin}$) is the minimal area of struts, and $^0L_{Smax}$ (and $^1L_{Smax}$) is the maximal length of struts, evaluated at Configuration 0 (and Configuration 1). The states of configurations are demonstrated in Fig. 4. The middle term in Eq. (20) is the actual critical stress before buckling, which shall be evaluated in the undeformed configuration (i.e. Configuration 0). However, in this research we are specifying the lengths and areas of members at the prestressed configuration (i.e. Configuration 1), thus the last term is used to provide an approximate upper bound for the compressive stress in struts, assuming that the strut material has a positive Poisson's ratio. Since ^1A_S and $^1L_{max}$ are given for the design, this lower bound is a function of E_S, which is plotted as the green lines in Figs. 6(c) and (d), normalized by E_C.

6 . Tunable elastodynamic bandgaps

Besides tunable *static* properties, the prestressed tensegrity metamaterials also provide tunable *dynamic* properties. Hence, tensegrity metamaterials can be used for applications such as impact absorption, vibration isolation, or acoustic cloaking [55, 56, 57]. In this paper, we focus on the phononic bandgaps of the tensegrity metamaterial, which are the frequency ranges prohibiting elastic wave propagation. The freedom provided by our design framework allows us to tailor the unit cells for better likelihood of bandgaps. For instance, the porous unit cell is comprised of voids in the tessellation that renders the system heterogeneous which could lead to bandgaps [56, 58].

Using the same tessellation blocks as in previous section, we are interested in finding all the free vibration modes of wave propagation in the infinite tensegrity metamaterials, by means of Bloch wave analysis. The free vibration modes of a structure are the eigenvectors of the generalized eigenvalue problem:

$$\mathbf{K}\mathbf{u} = \omega^2 \mathbf{M}\mathbf{u}, \tag{21}$$

where, $\mathbf{K}$ and $\mathbf{M}$ represent the stiffness and mass matrices of the infinite global system defined in the real space, and ω are the natural frequencies of harmonic wave propagation through the metamaterial. For periodic metamaterials consisting very large assembly of unit cells, direct evaluation of their eigenmodes is computationally intractable. To overcome this challenge, the dynamics of periodic structural systems is typically studied using the Bloch wave analysis [59, 58] framework, which reduces the generalized eigenvalue problem to that on a single unit cell, by virtue of Bloch's theorem and spatial Discrete Fourier Transform.

We calculate the eigenvalues of a reduced eigenvalue problem on the unit cell for each of the wavevectors defined in the *Irreducible Brillouin Zone* (IBZ) of the periodic system [58]:

$$\tilde{\mathbf{K}}_{\mathbf{m}}\tilde{\mathbf{u}}_{\mathbf{m}} = \omega^2 \tilde{\mathbf{M}}\tilde{\mathbf{u}}_{\mathbf{m}}, \quad \text{with,} \quad \tilde{\mathbf{K}}_{\mathbf{m}} = \sum_{\mathbf{n}=-\mathbf{1}}^{\mathbf{1}} e^{-\mathbf{i}\mathbf{k}_{\mathbf{m}}\cdot\mathbf{x}_{\mathbf{n}}}\mathbf{K}_{\mathbf{0n}}, \tag{22}$$

where, $\tilde{\mathbf{K}}_{\mathbf{m}}$ is the reduced stiffness matrix defined in the reciprocal space, which depends on the wavevector $\mathbf{k}_{\mathbf{m}}$ as shown above. The summation above goes over a reference unit cell as well as its immediate neighboring cells (with lattice position vectors $\mathbf{x}_{\mathbf{n}}$) of the tensegrity metamaterial. The matrix $\mathbf{K}_{\mathbf{0n}}$ is a matrix extracted from $\mathbf{K}$ with rows corresponding to the degrees-of-freedom

(DOFs) of the reference unit cell, and columns corresponding to the DOFs of the **n**-indexed unit cell. The matrix $\tilde{\mathbf{M}}$ is the diagonal mass matrix obtained using a lumped mass technique over the members in the unit cell.

Using Eq. 22, we can obtain the dispersion diagrams of the tensegrity metamaterials at any given level of prestress. For the sake of simplicity and clear presentation, here we focus on the wave propagation in 1D and 2D tessellations. However, the analysis framework is equally applicable to 3D tessellations.

We locate the bandgaps (if present) across the wavevectors in the IBZ at all the frequencies and for varying levels of prestress. Similar to the elastostatic properties, the frequency bandgaps also exhibit tunability in response to changing prestress, as demonstrated in Figs. 7 and 8. We observe that the one-dimensional dense tessellation has wider bandgaps at lower frequencies (e.g. between 0 to 2.5 kHz), compared to the two-dimensional dense tessellation. Similarly, the porous tessellations that possess voids result in wider bandgaps at lower frequencies, compared to the dense tessellations. In both cases, this is explained by the reduction of mobility restraint from neighboring unit cells leading to wider bandgaps at lower frequencies. The examples show that by varying the level of prestress, tensegrity metamaterials can provide versatile and tunable properties for acoustic applications.

7 . Conclusion

We present a design framework that allows for automated creation of tensegrity metamaterials. The proposed methodology begins by specifying a geometry of the tessellation block that tiles space according to primitive vectors. Then a tessellation block is designed within this geometry by topology optimization which considers the periodicity of the final system. This resulting tessellation block can be tessellated in various ways in space to create metamaterials. Together with the unit geometry, additional and optional procedures such as concavities, morphing, and various strategies for tessellation, provide a rich design space for tensegrity metamaterials. While the resulting tensegrity properties cannot be easily predicted, parametric analysis on a few of these techniques offer sufficient control for the purpose of the present work. We present a library of various designs of the tessellation block in Table A.1. Examples in the present work demonstrate how the static and dynamic properties of the tensegrity metamaterials designed using our approach can be tuned by changing the prestress level of the system.

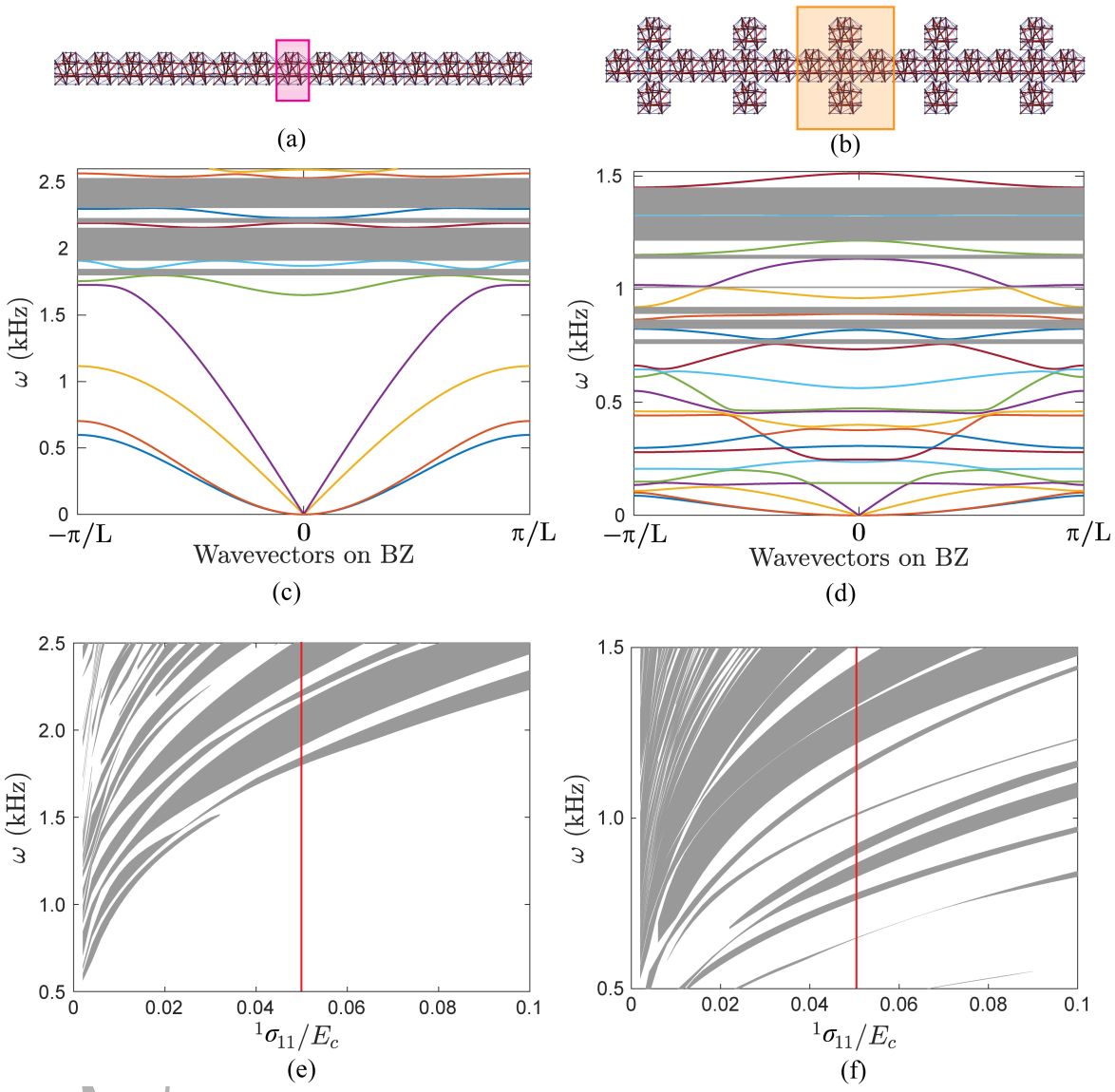

Figure 7: Schematics of the quasi one-dimensional tensegrity chains with **(a)** Dense and **(b)** Porous tensegrity unit cells (shown in shaded rectangles) and their corresponding variation of bandgaps with prestress shown in **(e)** and **(f)**. **(c)**, **(d)** Band structure diagrams at a prestress of $(0.05E_C)$ represented by red lines in **(e)** and **(f)**, respectively. The gray shaded regions illustrate the elastic bandgaps.

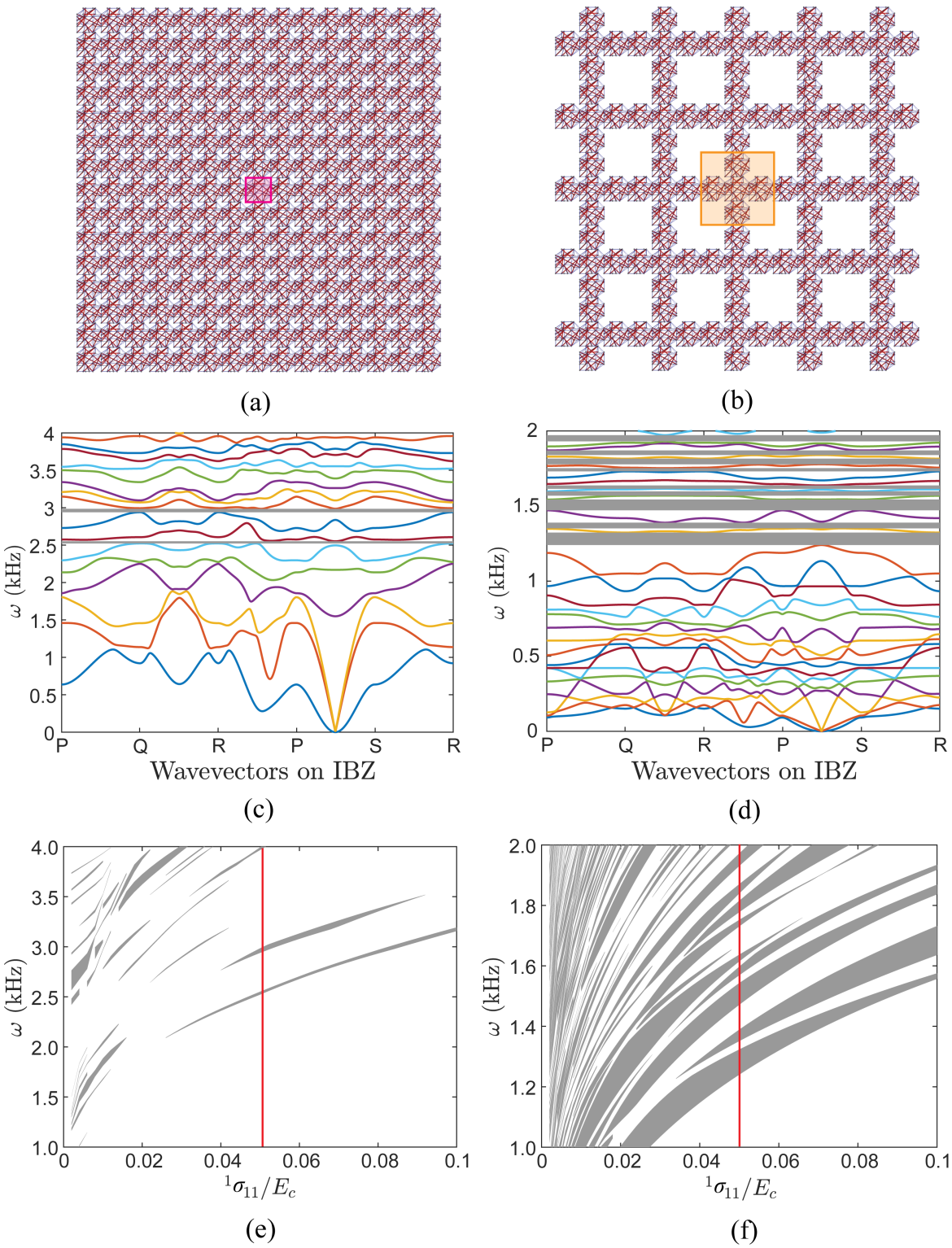

Figure 8: Schematics of the quasi two-dimensional tensegrity tessellations with **(a)** Dense and **(b)** Porous tensegrity unit cells (shown in shaded rectangles) and their corresponding variation of bandgaps with prestress shown in **(e)** and **(f)**. **(c)**, **(d)** Band structure diagrams at a prestress of $(0.05E_C)$ represented by red lines in **(e)** and **(f)**, respectively. The gray shaded regions illustrate the elastic bandgaps.

The current framework may be enhanced in the future by taking into account the mechanical properties of resultant metamaterial into the optimization formulation, and allowing the nodes to morph around in order to obtain simpler designs. However, such an objective or constraint is likely to lead to nonlinear integer programming problems. Therefore, how to efficiently solve those problems still poses a challenge. Moreover, the manufacturing of tensegrity metamaterials with properly induced prestress needs to be investigated. Additive manufacture technologies with the capability of printing multiple materials appear as the most promising at the time of this writing [60]. For example, we can print the cables and struts using two materials with different thermal expansion coefficients, and then by changing ambient temperature, the thermal deformation induced incompatibility can generate prestress in the system.

Acknowledgment

We acknowledge support from the US NSF (National Science Foundation) through Grants 1538830, and the Raymond Allen Jones Chair at the Georgia Institute of Technology. In addition, Ke Liu acknowledges support of the China Scholarship Council (CSC). The authors also acknowledge Dr. Raj K. Pal for helpful discussion about computational homogenization during the development of this research.

Appendix A. Library of tensegrity tessellation blocks

In Table A.1, we provide ten different tessellation blocks that can create space-spanning tessellations. The "Specification" column provides some detailed information about each design. As a matter of notation, R_{rz} is the radius of the spherical restriction zone located at the centroid of each unit geometry, N_B is the total number of members (including struts and cables), N_S is the number of struts in the tessellation block (a subset of N_B), and "Class" denotes the resulting global Class category of the tensegrity metamaterial. The behavior of a tensegrity structure depends on the number of independent prestressed states (self-stresses) and its kinematic indeterminacy (independent internal mechanisms), which are denoted by PS and KI, respectively [11]. Notice that the tessellation block for the Cube design domain is Class-1, however, the resulting metamaterial is Class-4.

Table A.1: Tensegrity tessellations

Design Domain	Vertices	Primitive Vectors (columns)	Assembly Sample	Specifications	Tessellation Block
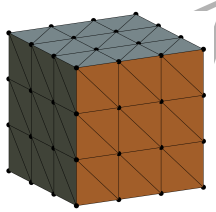 Cube	$\mathbf{v}_{1\to 8} = [\pm 1, \quad \pm 1, \quad \pm 1]$	$\mathbf{A}_1 = \begin{bmatrix} 2, & 0, & 0 \\ 0, & 2, & 0 \\ 0, & 0, & 2 \end{bmatrix}$	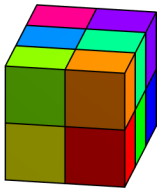	$R_{rz} = 0.1$ $N_S = 24$ Class-4 N_V=48,N_B=120 KI=25, PS=7	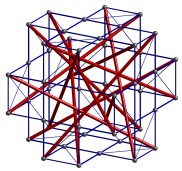
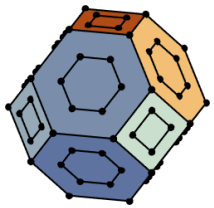 Truncated Octahedron	$\mathbf{v}_{1\to 24} = \text{perm}\,[0, \quad \pm 1, \quad \pm 2]$	$\mathbf{A}_1 = \begin{bmatrix} 2, & 2, & 2 \\ -2, & 2, & 2 \\ 2, & -2, & 2 \end{bmatrix}$		$R_{rz} = 0.75$ $N_S = 24$ Class-1 N_V=58,N_B=178 KI=14, PS=24	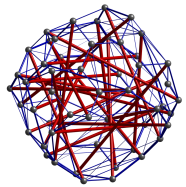
		$\mathbf{A}_2 = 4 \cdot \begin{bmatrix} 1, & 0, & 0 \\ 0, & 1, & 0 \\ 0, & 0, & 1 \end{bmatrix}$	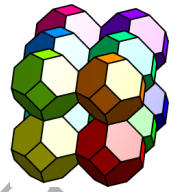	$R_{rz} = 0.75$ $N_S = 24$ Class-1 N_V=73,N_B=204 KI=32, PS=23	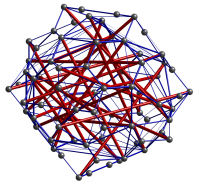
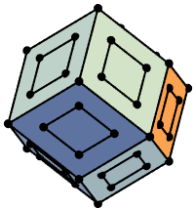 Rhombic Dodecahedron	$\mathbf{v}_{1\to 8} = [\pm 1, \quad \pm 1, \quad \pm 1]$ $\mathbf{v}_{9\to 10} = [\pm 1, \quad 0, \quad 0]$ $\mathbf{v}_{11\to 12} = [0, \quad \pm 1, \quad 0]$ $\mathbf{v}_{13\to 14} = [0, \quad 0, \quad \pm 1]$	$\mathbf{A}_1 = \begin{bmatrix} 2, & 2, & 0 \\ 2, & -2, & 0 \\ 2, & 0, & 2 \end{bmatrix}$		$R_{rz} = 0.5$ $N_S = 20$ Class-1 N_V=44,N_B=138 KI=8, PS=20	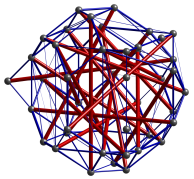

ACCEPTED MANUSCRIPT

Table A.1: (continued)

Design Domain	Vertices	Primitive Vectors (columns)	Assembly Sample	Specifications	Tessellation Block
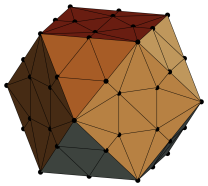 Cuboctahedron	$\mathbf{v}_{1\to4} = [\pm1 \quad , \quad \pm1 \quad , \quad 0]$ $\mathbf{v}_{5\to8} = [\pm1 \quad , \quad 0 \quad , \quad \pm1]$ $\mathbf{v}_{9\to12} = [0 \quad , \quad \pm1 \quad , \quad \pm1]$	$\mathbf{A}_1 = \begin{bmatrix} 2 & , & 0 & , & 0 \\ 0 & , & 2 & , & 0 \\ 0 & , & 0 & , & 2 \end{bmatrix}$	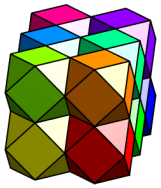	$R_{rz} = 0.75$ $N_S = 13$ Class-1 N_V=40,N_B=109 KI=17, PS=12	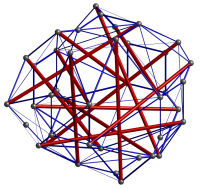
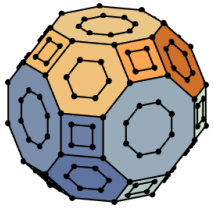 Truncated Cuboctahedron	$\phi_1 = 1 + \sqrt{2}$ $\phi_2 = 1 + 2\sqrt{2}$ $\phi_3 = 2 + 2\sqrt{2}$ $\phi_4 = 2 + 3\sqrt{2}$ $\mathbf{v}_{1\to48} = \text{perm}\,[\pm1, \quad \pm\phi_1, \quad \pm\phi_2]$	$\mathbf{A}_1 = 2\phi_2 \cdot \begin{bmatrix} 1, & 0, & 0 \\ 0, & 1, & 0 \\ 0, & 0, & 1 \end{bmatrix}$	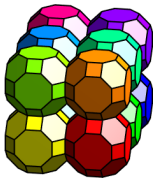	$R_{rz} = 1.5$ $N_S = 24$ Class-1 N_V=108,N_B=271 KI=70, PS=23	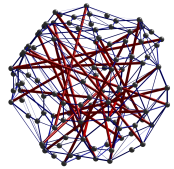
		$\mathbf{A}_2 = \phi_3 \cdot \begin{bmatrix} 1, & 1, & 1 \\ -1, & 1, & 1 \\ 1, & -1, & 1 \end{bmatrix}$		$R_{rz} = 1.5$ $N_S = 24$ Class-1 N_V=128,N_B=310 KI=90, PS=22	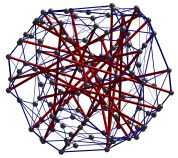
		$\mathbf{A}_3 = \phi_4 \cdot \begin{bmatrix} 1, & 1, & 0 \\ -1, & 1, & 0 \\ 1, & 0, & 1 \end{bmatrix}$		$R_{rz} = 1.5$ $N_S = 24$ Class-1 N_V=137,N_B=329 KI=100, PS=24	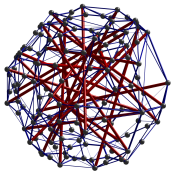

ACCEPTED MANUSCRIPT

Table A.1: (continued)

Design Domain	Vertices	Primitive Vectors (columns)	Assembly Sample	Specifications	Tessellation Block
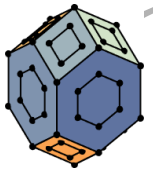 Elongated Dodecahedron	$\phi = 1/\sqrt{3}$ $\mathbf{v}_{1\to8} = [\pm1, \quad \pm1, \quad \pm\phi]$ $\mathbf{v}_{9\to12} = [\pm1, \quad 0, \quad \pm2\phi]$ $\mathbf{v}_{13\to16} = [0, \quad \pm1, \quad \pm2\phi]$ $\mathbf{v}_{17\to18} = [0, \quad 0, \quad \pm\sqrt{3}]$	$\mathbf{A}_1 = \begin{bmatrix} 2, & 0, & 0 \\ 0, & 2, & 0 \\ 1, & 1, & 4\phi \end{bmatrix}$	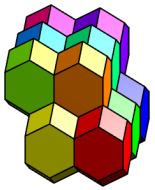	$R_{rz} = 0.5$ $N_S = 24$ Class-1 N_V=48,N_B=155 KI=5, PS=22	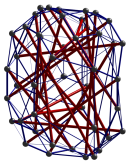
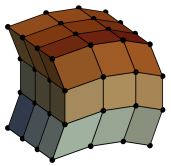 Morphed Cube	$\mathbf{v}_{1\to8} = [\pm1, \quad \pm1, \quad \pm1]$	$\mathbf{A}_1 = \begin{bmatrix} 2, & 0, & 0 \\ 0, & 2, & 0 \\ 0, & 0, & 2 \end{bmatrix}$	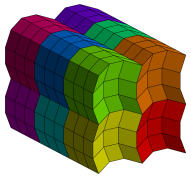	$N_S = 24$ Class-1 N_V=26,N_B=75 KI=5, PS=8	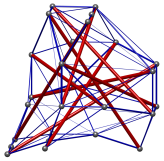

ACCEPTED MANUSCRIPT

Appendix B. Computation of identification matrix M

First, we need to find pairs of boundary nodes that are images of each other under translational symmetry. Assume that the primitive vectors are $\boldsymbol{a}_1$, $\boldsymbol{a}_2$, and $\boldsymbol{a}_3$. We can translate the unit cell nodal coordinates by different combinations of primitive vectors. If a node after the translation has the same coordinate as another node before the translation; these two nodes are identified as a pair. Supposing that there are m pairs of identified nodes, we can store their nodal incidence in a $m \times 2$ array.

Second, we use a union-find algorithm [61] with path compression and weighting to obtain the independent groups of nodes, as well as the identification matrix $\mathbf{Q}$. The MATLAB code for this algorithm is given below. The input array `SameNodePairs` contains the indices of the identified pairs, and where `Nv` is refer as N_V. The output array `Q` is the identification matrix $\mathbf{Q}$, and the array `Pairs` is a $N_V \times 2$ matrix with the pairs of identified nodes.

```
function [Q,Pairs] = CondenseTopMat(SameNodePairs,Nv)
% union-find algorithm with path compression and weighting
id = 1:Nv;
sz = ones(1,Nv);

FirstNd = SameNodePairs(:,1);
SecondNd = SameNodePairs(:,2);

for i = 1:length(FirstNd)
    % make every node in path point to its grandparent (path compression)
    FNdi = FirstNd(i);
    while FNdi ≠ id(FNdi)
        id(FNdi) = id(id(FNdi));
        FNdi = id(FNdi);
    end
    SNdi = SecondNd(i);
    while SNdi ≠ id(SNdi)
        id(SNdi) = id(id(SNdi));
        SNdi = id(SNdi);
    end

    % merge smaller tree into larger tree (weighted quick union)
    if FNdi ≠ SNdi
        if sz(FNdi) < sz(SNdi)
            id(FNdi) = SNdi;
            sz(SNdi) = sz(SNdi) + sz(FNdi);
        else
            id(SNdi) = FNdi;
            sz(FNdi) = sz(FNdi) + sz(SNdi);
        end
    end
end
```

```
33
34 % Compress to root
35 for i = Nv
36     while id(i)≠id(id(i))
37         id(i) = id(id(i));
38     end
39 end
40 Pairs = [id;(1:Nv)]';
41
42 idnew = id; iduni = unique(id);
43 for i = 1:numel(unique(id))
44     idnew(id==iduni(i)) = i;
45 end
46 Q = sparse(1:Nv,idnew,ones(Nv,1),Nv,numel(unique(idnew)));
47 return
```

Appendix C. Computation of effective elasticity tensor

We write a MATLAB function to implement the homogenization procedure as explained in [53]. The input arguments are: array of nodal coordinates (`NODE`); array of member connectivities (`BARS`); array of three primitive vectors (`Amat`); array of prestress forces (`P`); array of member areas (`A`); array of Young's modulus of all members `E`; the identification matrix (`Q`); and identified pairs of nodes (`Pairs`). The output array `Dhom` is the homogenized elasticity tensor $\mathbf{D}$. The function also gives the six deformation modes (stored in `Modes`) of the unit cell under six elementary displacement-type boundary conditions, corresponding to three uniaxial extensions and three pure shear loadings. Denoting $\mathbf{S}$ as the elastic compliance, we have $\mathbf{S} = \mathbf{D}^{-1}$. The Poisson's ratio ν_{12} is derived as [62]:

$$\nu_{12} = -\frac{{}^{1}\varepsilon_{22}}{{}^{1}\varepsilon_{11}} = -\frac{S_{12}}{S_{11}}. \tag{C.1}$$

```
1  function [Dhom, Modes] = GetHomProp(NODE,BARS,Amat,P,A,E,Q,Pairs)
2  %% Get unit cell full stiffness matrix Kuc
3  Nv = size(NODE,1);
4  Nb = size(BARS,1);
5  % Length vector and equilibrium matrix
6  D = [NODE(BARS(:,2),1) - NODE(BARS(:,1),1),...
7       NODE(BARS(:,2),2) - NODE(BARS(:,1),2),...
8       NODE(BARS(:,2),3) - NODE(BARS(:,1),3)];
9  L = sqrt(D(:,1).^2 + D(:,2).^2 + D(:,3).^2);
10 D = [D(:,1)./L D(:,2)./L D(:,3)./L];
11 B = sparse(repmat((1:Nb)',1,6),[3*BARS(:,1)-2 3*BARS(:,1)-1 3*BARS(:,1),...
12     3*BARS(:,2)-2 3*BARS(:,2)-1 3*BARS(:,2)],[D -D],Nb,3*Nv);
13 % Linear elastic stiffness matrix
14 Ke = B' * sparse(1:Nb,1:Nb,(E.*A./L)) * B;
15 % Geometric Stiffness Matrix
```

```
G = sparse([1:Nb,1:Nb],reshape(BARS,[],1),[ones(Nb,1);-ones(Nb,1)],Nb,Nv);
Kg = kron((G'*sparse(1:Nb,1:Nb,P./L)*G),speye(3));
% Assembly unit cell stiffness matrix
Kuc = Ke + Kg;
% Eliminate numerical rounding errors
Kuc = 0.5 * (Kuc + Kuc');

%% Get homogenized elasticity tensor
B0 = kron(Q,eye(3));
Bep = ...
    [Amat(1,1),         0,         0, Amat(2,1)/2,           0, Amat(3,1)/2;
             0, Amat(2,1),         0, Amat(1,1)/2, Amat(3,1)/2,           0;
             0,         0, Amat(3,1),           0, Amat(2,1)/2, Amat(1,1)/2;
     Amat(1,2),         0,         0, Amat(2,2)/2,           0, Amat(3,2)/2;
             0, Amat(2,2),         0, Amat(1,2)/2, Amat(3,2)/2,           0;
             0,         0, Amat(3,2),           0, Amat(2,2)/2, Amat(1,2)/2;
     Amat(1,3),         0,         0, Amat(2,3)/2,           0, Amat(3,3)/2;
             0, Amat(2,3),         0, Amat(1,3)/2, Amat(3,3)/2,           0;
             0,         0, Amat(3,3),           0, Amat(2,3)/2, Amat(1,3)/2];
BaTopInt = Amat \ (NODE(Pairs(:,2),:) - NODE(Pairs(:,1),:))';
BaTopInt(abs(BaTopInt)<1e-3) = 0;
BaTop = sign(BaTopInt)';
Ba = kron(BaTop,eye(3));
Nrn = size(B0,2);
D0 = -pinv(full(B0'*Kuc*B0)) * (B0'*Kuc*Ba); % Pseudo inverse
Da = B0*D0 + Ba;
Kda = Da' * Kuc * Da;
Dhom = Bep' * Kda * Bep / det(Amat);
Modes = Da * Bep;
return
```

References

[1] Y. Tamura, I. Hatta, T. Matsuda, H. Sugi, T. Tsuchiya, Changes in muscle stiffness during contraction recorded using ultrasonic waves, Nature 299 (1982) 631–633.

[2] G. J. C. Ettema, P. A. Huijing, Skeletal muscle stiffness in static and dynamic contractions, Journal of Biomechanics 27 (11) (1994) 1361–1368.

[3] I. V. Ogneva, D. V. Lebedev, B. S. Shenkman, Transversal stiffness and Young's Modulus of single fibers from rat Soleus muscle probed by Atomic Force Microscopy, Biophysical Journal 98 (3) (2010) 418–424.

[4] D. E. Ingber, The architecture of life, Scientific American 278 (1) (1998) 48–57.

[5] T. Liedl, B. Högberg, J. Tytell, D. E. Ingber, W. M. Shih, Self-assembly of three-dimensional prestressed tensegrity structures from DNA, Nature Nanotechnology 5 (2010) 520–524.

[6] G. Scarr, Biotensegrity: The structural basis of life, Handspring Publishing, 2014.

[7] K. Liu, J. Wu, G. H. Paulino, H. J. Qi, Programmable deployment of tensegrity structures by stimulus-responsive polymers, Scientific Reports 7 (2017) 3511.

[8] C. R. Calladine, Buckminster Fuller's "Tensegrity" structures and Clerk Maxwell's rules for the construction of stiff frames, International Journal of Solids and Structures 14 (2) (1978) 161–172.

[9] R. Motro, Tensegrity: Structural Systems for the Future, Butterworth-Heinemann, London, 2006.

[10] R. E. Skelton, M. de Oliveira, Tensegrity Systems, Springer US, New York, 2009.

[11] J. Y. Zhang, M. Ohsaki, Tensegrity Structures - Form, Stability, and Symmetry, Springer Japan, Tokyo, 2015.

[12] S. D. Guest, The stiffness of tensegrity structures, IMA Journal of Applied Mathematics 76 (2011) 57–66.

[13] E. Heartney, K. Snelson, Kenneth Snelson: Forces Made Visible, Hudson Hills, 2009.

[14] A. G. Tibert, S. Pellegrino, Deployable tensegrity reflectors for small satellites, Journal of Spacecraft and Rockets 39 (5) (2002) 701–709.

[15] S. Pellegrino, Deployable structures, Springer-Verlag Wien, New York, 2001.

[16] K. Caluwaerts, J. Despraz, A. Içen, A. P. Sabelhaus, J. Bruce, B. Schrauwen, V. SunSpiral, Design and control of compliant tensegrity robots through simulation and hardware validation, Journal of The Royal Society Interface 11 (98) (2014) 1–13.

[17] K. Kim, A. K. Agogino, D. Moon, L. Taneja, A. Toghyan, B. Dehghani, V. SunSpiral, A. M. Agogino, Rapid prototyping design and control of tensegrity soft robot for locomotion, in: 2014 IEEE International Conference on Robotics and Biomimetics (ROBIO 2014), 2014.

[18] K. W. Moored, T. H. Kemp, N. E. Houle, H. Bart-Smith, Analytical predictions, optimization, and design of a tensegrity-based artificial pectoral fin, International Journal of Solids and Structures 48 (22–23) (2011) 3142–3159.

[19] S. Pellegrino, A class of tensegrity domes, International Journal of Space and Structures 7 (2) (1992) 127–142.

[20] X. Y. Zheng, H. Lee, T. H. Weisgraber, M. Shusteff, J. DeOtte, E. B. Duoss, J. D. Kuntz, M. M. Biener, Q. Ge, J. A. Jackson, S. O. Kucheyev, N. X. Fang, C. M. Spadaccini, Ultralight, ultrastiff mechanical metamaterials, Science 344 (6190) (2014) 1373–1377.

[21] L. R. Meza, S. Das, J. R. Greer, Strong, lightweight, and recoverable three-dimensional ceramic nanolattices, Science 345 (6202) (2014) 1322–1326.

[22] J. Christensen, M. Kadic, O. Kraft, M. Wegener, Vibrant times for mechanical metamaterials, MRS Communications 5 (3) (2015) 453–462.

[23] T. A. Schaedler, W. B. Carter, Architected cellular materials, Annual Review of Materials Research 46 (1) (2016) 187–210.

[24] F. Fraternali, L. Senatore, C. Daraio, Solitary waves on tensegrity lattices, Journal of the Mechanics and Physics of Solids 60 (6) (2012) 1137–1144.

[25] F. Fraternali, G. Carpentieri, A. Amendola, R. E. Skelton, V. F. Nesterenko, Multiscale tunability of solitary wave dynamics in tensegrity metamaterials, Applied Physics Letters 105 (2014) 201903.

[26] J. J. Rimoli, R. K. Pal, Mechanical response of 3-dimensional tensegrity lattices, Composites Part B: Engineering 115 (2016) 30–42.

[27] F. Fabbrocino, G. Carpentieri, Three-dimensional modeling of the wave dynamics of tensegrity lattices, Composite Structures 173 (2017) 9–16.

[28] A. Al Sabouni-Zawadzka, W. Gilewski, Smart metamaterial based on the simplex tensegrity pattern, Materials 11 (5) (2018) 673.

[29] Q. Zhang, Y. Dobah, F. Scarpa, F. Fraternali, R. E. Skelton, Tensegrity cell mechanical metamaterial with metal rubber, Applied Physics Letters 113 (3) (2018) 031906.

[30] R. K. Pal, M. Ruzzene, J. J. Rimoli, Tunable wave propagation by varying prestrain in tensegrity-based periodic media, Extreme Mechanics Letters 22 (2018) 149–156.

[31] A. Amendola, A. Krushynska, C. Daraio, N. M. Pugno, F. Fraternali, Tuning frequency band gaps of tensegrity mass-spring chains with local and global prestress, International Journal of Solids and Structures (2018) 155 (2018) 47–56.

[32] Y. Li, X.-Q. Feng, Y.-P. Cao, H. Gao, Constructing tensegrity structures from one-bar elementary cells, Proceedings of the Royal Society A 466 (2113) (2010) 45–61.

[33] T. Tachi, Interactive Freeform Design of Tensegrity, in: L. Hesselgren, S. Sharma, J. Wallner, N. Baldassini, P. Bompas, J. Raynaud (Eds.), Advances in Architectural Geometry 2012, Springer Vienna, 2013, pp. 259–268.

[34] J. Y. Zhang, M. Ohsaki, Adaptive force density method for form-finding problem of tensegrity structures, International Journal of Solids and Structures 43 (18–19) (2006) 5658–5673.

[35] M. Ohsaki, J. Zhang, Nonlinear programming approach to form-finding and folding analysis of tensegrity structures using fictitious material properties, International Journal of Solids and Structures 69–70 (2015) 1–10.

[36] S. Lee, J. Lee, Advanced automatic grouping for form-finding of tensegrity structures, Structural and Multidisciplinary Optimization 55 (3) (2016) 959–968.

[37] S. Ehara, Y. Kanno, Topology design of tensegrity structures via mixed integer programming, International Journal of Solids and Structures 47 (5) (2010) 571–579.

[38] Y. Kanno, Topology optimization of tensegrity structures under self-weight loads, Journal of the Operations Research Society of Japan 55 (2) (2012) 125–145.

[39] Y. Kanno, Topology optimization of tensegrity structures under compliance constraint: A mixed integer linear programming approach, Optimization and Engineering 14 (1) (2013) 61–96.

[40] Y. Kanno, Exploring new tensegrity structures via mixed integer programming, Structural and Multidisciplinary Optimization 48 (1) (2013) 95–114.

[41] X. Xu, Y. Wang, Y. Luo, A. M. Asce, General approach for topology-finding of tensegrity structures, Journal of Structural Engineering 142 (10) (2016) 04016061.

[42] N. Pietroni, M. Tarini, A. Vaxman, D. Panozzo, P. Cignoni, Position-based tensegrity design, ACM Transactions on Graphics 36 (6) (2017) 172.

[43] K. Liu, G. H. Paulino, Tensegrity topology optimization by force maximization on arbitrary ground structures, Structural and Multidisciplinary Optimization 59 (6) (2019) 2041–2062.

[44] Y. Li, X.-Q. Feng, Y.-P. Cao, H. Gao, A Monte Carlo form-finding method for large scale regular and irregular tensegrity structures, International Journal of Solids and Structures 47 (14–15) (2010) 1888–1898.

[45] W. S. Dorn, R. E. Gomory, H. J. Greenberg, Automatic Design of Optimal Structures, Journal de Mecanique 3 (1) (1964) 25–52.

[46] O. D. S. Smith, Generation of ground structures for 2D and 3D design domains, Engineering Computations 15 (4) (1998) 462–500.

[47] T. Zegard, G. H. Paulino, GRAND – Ground structure based topology optimization for arbitrary 2D domains using MATLAB, Structural and Multidisciplinary Optimization 50 (5) (2014) 861–882.

[48] T. Zegard, G. H. Paulino, GRAND3 – Ground structure based topology optimization for arbitrary 3D domains using MATLAB, Structural and Multidisciplinary Optimization 52 (6) (2015) 1161–1184.

[49] F. P. Preparata, M. I. Shamos, Computational Geometry: An Introduction, Springer, New York, 1993.

[50] M. de Berg, O. Cheong, M. van Kreveld, M. Overmars, Computational Geometry: Algorithms and Applications, 3rd Edition, Springer, Berlin, 2008.

[51] K.-J. Bathe, Finite element procedures, 2nd Edition, Klaus-Jrgen Bathe, 2014.

[52] B. Hassani, E. Hinton, Homogenization and Structural Topology Optimization: Theory, Practice and Software, Springer-Verlag London, London, 1999.

[53] A. Vigliotti, D. Pasini, Stiffness and strength of tridimensional periodic lattices, Computer Methods in Applied Mechanics and Engineering 229–232 (2012) 27–43.

[54] S. P. Timoshenko, J. M. Gere, Theory of elastic stability, 2nd Edition, Dover Publications, New York, 2009.

[55] M. Maldovan, Sound and heat revolutions in phononics, Nature 503 (2013) 209–217.

[56] M. I. Hussein, M. J. Leamy, M. Ruzzene, Dynamics of phononic materials and structures: historical origins, recent progress, and future outlook, Applied Mechanics Reviews 66 (4) (2014) 040802.

[57] P. Wang, F. Casadei, S. Shan, J. C. Weaver, K. Bertoldi, Harnessing buckling to design tunable locally resonant acoustic metamaterials, Physical Review Letters 113 (1) (2014) 014301.

[58] P. P. Pratapa, P. Suryanarayana, G. H. Paulino, Bloch wave framework for structures with nonlocal interactions: Application to the design of origami acoustic metamaterials, Journal of the Mechanics and Physics of Solids 118 (2018) 115–132.

[59] A. S. Phani, J. Woodhouse, N. A. Fleck, Wave propagation in two-dimensional periodic lattices, The Journal of the Acoustical Society of America 119 (4) (2006) 1995–2005.

[60] Q. Wang, J. A. Jackson, Q. Ge, J. B. Hopkins, C. M. Spadaccini, N. X. Fang, Lightweight mechanical metamaterials with tunable negative thermal expansion, Physical Review Letters 117 (2016) 175901.

[61] R. Sedgewick, K. Wayne, Algorithms, 4th Edition, Addison-Wesley Professional, New Jersey, 2011.

[62] T. C. T. Ting, T. Chen, Poisson's ratio for anisotropic elastic materials can have no bounds, Quarterly Journal of Mechanics and Applied Mathematics 58 (1) (2005) 73–82.